Nano-Micro Letters

ISSN 2311-6706
e-ISSN 2150-5551
CN 31-2103/TB

ARTICLE

https://doi.org/10.1007/s40820-019-0278-9

Cite as
Nano-Micro Lett.
(2019) 11:49

Received: 15 April 2019
Accepted: 14 May 2019
Published online: 6 June 2019

Novel Insights into Energy Storage Mechanism of Aqueous Rechargeable Zn/MnO_2 Batteries with Participation of Mn^{2+}

Yongfeng Huang[1,2], Jian Mou[1], Wenbao Liu[1,2], Xianli Wang[1], Liubing Dong[1] ✉, Feiyu Kang[1,2] ✉, Chengjun Xu[1] ✉

Yongfeng Huang and Jian Mou have contributed equally to this work.

✉ Liubing Dong, dong1060@126.com; Feiyu Kang, fykang@mail.tsinghua.edu.cn; Chengjun Xu, vivaxuchengjun@163.com

[1] Shenzhen Geim Graphene Center, Graduate School at Shenzhen, Tsinghua University, Shenzhen 518055, People's Republic of China

[2] State Key Laboratory of New Ceramics and Fine Processing, School of Materials Science and Engineering, Tsinghua University, Beijing 100084, People's Republic of China

HIGHLIGHTS

- Pourbaix diagram of Mn–Zn–H_2O system was used to analyze the charge–discharge processes of Zn/MnO_2 batteries.
- Electrochemical reactions with the participation of various ions inside Zn/MnO_2 batteries were revealed.
- A detailed explanation of phase evolution inside Zn/MnO_2 batteries was provided.

ABSTRACT Aqueous rechargeable Zn/MnO_2 zinc-ion batteries (ZIBs) are reviving recently due to their low cost, non-toxicity, and natural abundance. However, their energy storage mechanism remains controversial due to their complicated electrochemical reactions. Meanwhile, to achieve satisfactory cyclic stability and rate performance of the Zn/MnO_2 ZIBs, Mn^{2+} is introduced in the electrolyte (e.g., $ZnSO_4$ solution), which leads to more complicated reactions inside the ZIBs systems. Herein, based on comprehensive analysis methods including electrochemical analysis and Pourbaix diagram, we provide novel insights into the energy storage mechanism of Zn/MnO_2 batteries in the presence of Mn^{2+}. A complex series of electrochemical reactions with the co-participation of Zn^{2+}, H^+, Mn^{2+}, SO_4^{2-}, and OH^- were revealed. During the first discharge process, co-insertion of Zn^{2+} and H^+ promotes the transformation of MnO_2 into Zn_xMnO_4, MnOOH, and Mn_2O_3, accompanying with increased electrolyte pH and the formation of $ZnSO_4{\cdot}3Zn(OH)_2{\cdot}5H_2O$. During the subsequent charge process, Zn_xMnO_4, MnOOH, and Mn_2O_3 revert to α-MnO_2 with the extraction of Zn^{2+} and H^+, while $ZnSO_4{\cdot}3Zn(OH)_2{\cdot}5H_2O$ reacts with Mn^{2+} to form $ZnMn_3O_7{\cdot}3H_2O$. In the following charge/discharge processes, besides aforementioned electrochemical reactions, Zn^{2+} reversibly insert into/extract from α-MnO_2, Zn_xMnO_4, and $ZnMn_3O_7{\cdot}3H_2O$ hosts; $ZnSO_4{\cdot}3Zn(OH)_2{\cdot}5H_2O$, $Zn_2Mn_3O_8$, and $ZnMn_2O_4$ convert mutually with the participation of Mn^{2+}. This work is believed to provide theoretical guidance for further research on high-performance ZIBs.

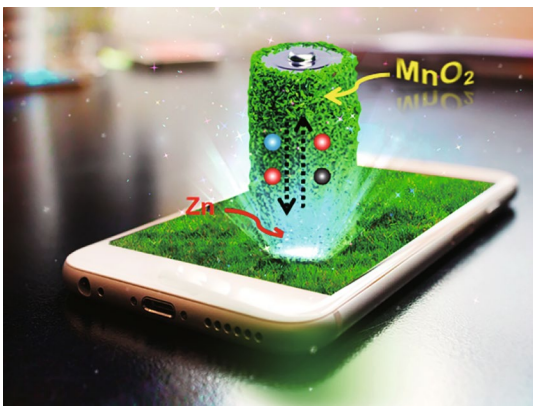

KEYWORDS Zinc-ion battery; MnO_2 cathode; Energy storage mechanism; Phase evolution

1 Introduction

Lithium-ion batteries (LIBs) have been widely used in consumer electronics due to high energy density, portability, and some other merits [1–4], whereas their security concerns and high cost restrict their large-scale applications in stationary grid storage and electric vehicles [5, 6]. Therefore, much attention has been paid to seek safe, eco-friendly, low-cost, and high-performance battery systems [6, 7]. Aqueous rechargeable zinc-ion batteries (ZIBs) are developed as a battery system, in which low-cost, non-toxic, and naturally abundant zinc metal is used as an anode and environment-friendly neutral aqueous Zn^{2+}-containing solution serves as electrolyte [8]. In recent years, a series of high-performance cathode materials for ZIBs have also been studied such as Prussian blue analog [9–11], vanadium oxides [12–19], manganese oxides [20–28], and some metal sulfides [29–31]. Among these materials, MnO_2 is particularly concerned for its high theoretical specific capacity, low cost, eco-friendliness, and diverse crystallographic polymorphs (e.g., α-MnO_2, δ-MnO_2, and γ-MnO_2) [27, 28, 32].

Many efforts have been made to reveal the energy storage mechanisms of Zn/MnO_2 ZIBs. Up to now, three types of energy storage mechanisms were proposed, including (i) Zn^{2+} insertion/extraction into/from MnO_2 [8, 33–36], (ii) conversion between MnO_2 and MnOOH with the participation of H^+ [37], and (iii) co-insertion of H^+ and Zn^{2+} [38]. Mechanisms (i) and (ii) explain the formation of $ZnMn_2O_4$ and MnOOH as discharging products on MnO_2 cathode in ZIBs, respectively, while cannot explain that there are two redox processes during one charge/discharge cycle of ZIBs. Mechanism (iii) seems to be capable of explaining the coexistence of $ZnMn_2O_4$ and MnOOH as discharging products on MnO_2 cathode, but deeper analysis will find that it is not accurate: The mechanism deems that potential of Zn^{2+} insertion is lower than that of H^+ insertion (this means that MnOOH forms before $ZnMn_2O_4$ once the battery discharge process begins), being conflicted to the experimental result that MnOOH appears latter than $ZnMn_2O_4$. In short, the current mechanisms are unsatisfactory to explain genuine charge/discharge process in ZIBs, mainly because they were proposed based on a simplistic view that the insertion of Zn^{2+} and H^+ and the phase change from MnO_2 to $ZnMn_2O_4$ or MnOOH are highly reversible. Furthermore, to achieve satisfactory cyclic stability and rate performance of the Zn/MnO_2 ZIBs, Mn^{2+} ions are always introduced in the electrolyte [37]. However, electrochemical reactions inside the ZIBs become more complicated in such cases, thus corresponding energy storage mechanism has not been clearly revealed. Therefore, it is necessary to re-examine the thermodynamic and kinetic characteristics of Zn/MnO_2 ZIBs to propose a reasonable Zn^{2+} storage mechanism.

In fact, for the active materials in aqueous ZIBs and some other rechargeable aqueous batteries, their structure and phase generally undergo complex changes during charge/discharge processes (e.g., the active materials can interact with not only metal ions, but also H^+, OH^-, and water molecules) [39]. This is an important reason why the energy storage mechanism of MnO_2 cathode in ZIBs is still inconclusive [40–43]. Besides general experimental techniques such as cyclic voltammetry (CV) and galvanostatic charge–discharge (GCD) tests, Pourbaix diagram (E-pH diagram) has been widely used to study electrochemical reactions in aqueous solution [44–47]. The electrochemical reductive products of active materials can be predicted according to the thermodynamics, which is beneficial for us to understand the charge/discharge process. Therefore, we combined experimental methods with the E-pH diagram of the Mn–Zn–H_2O system together to comprehensively analyze the charge/discharge processes of MnO_2 cathode in ZIBs and tried to reveal the authentic energy storage mechanism.

Herein, based on comprehensive analysis methods including electrochemical analysis and E-pH diagram, etc., we provide novel insights into the energy storage mechanism of Zn/MnO_2 batteries with the co-participation of Zn^{2+}, H^+, Mn^{2+}, SO_4^{2-}, and OH^-. During the first discharge process, co-insertion of Zn^{2+} and H^+ promotes the transformation of MnO_2 into Zn_xMnO_4, MnOOH, and Mn_2O_3, accompanying with increased electrolyte pH and the formation of $ZnSO_4{\cdot}3Zn(OH)_2{\cdot}5H_2O$ (noted as "BZSP"). During the subsequent charge process, Zn_xMnO_4, MnOOH, and Mn_2O_3 revert to α-MnO_2 with the extraction of Zn^{2+} and H^+, while BZSP reacts with Mn^{2+} to form $ZnMn_3O_7{\cdot}3H_2O$. In the following charge/discharge processes, besides aforementioned electrochemical reactions, Zn^{2+} reversibly inserts into/extract from α-MnO_2, Zn_xMnO_4, and $ZnMn_3O_7{\cdot}3H_2O$ hosts, and BZSP, $Zn_2Mn_3O_8$, and $ZnMn_2O_4$ convert mutually with the participation of Mn^{2+}. This work is believed to provide theoretical guidance for further research on high-performance ZIBs.

https://doi.org/10.1007/s40820-019-0278-9

2 Experimental

2.1 Material Synthesis

MnO_2 cathode material was synthesized through a chemical co-precipitation method. One hundred and fifty milliliters of 0.1 M $MnSO_4$ aqueous solution was dropped into 100 mL of $KMnO_4$ (0.1 M) solution under magnetic stirring, followed by continuous stirring for 6 h at room temperature. The resulting precipitate was filtered, washed repeatedly with deionized water, and dried at 80 °C for 12 h. The obtained sample was thoroughly ground in an agate mortar and then annealed at 400 °C for 5 h in air atmosphere. Note that we applied the heat treatment to improve the crystalline of MnO_2 because this makes it easier for us to use X-ray diffraction (XRD) and transmission electron microscopy (TEM) to detect the phase evolution of MnO_2 cathode during charge/discharge processes.

2.2 Electrochemical Characterizations

The cathode was prepared by coating a mixture paste of 70 wt% of MnO_2 powder, 20 wt% of acetylene black, and 10 wt% of LA133 binder on a stainless steel foil and dried overnight under vacuum conditions at 80 °C. In the prepared cathode, the mass loading of MnO_2 is around 1 mg cm^{-2}. Zn/MnO_2 ZIBs were assembled based on MnO_2 cathode, metallic Zn foil anode, air-laid paper separator, and zinc salt solution electrolyte (2 M $ZnSO_4$ or 2 M $ZnSO_4$ +0.5 M $MnSO_4$ solution).

The assembled ZIBs were kept more than 4 h before electrochemical measurements. The CV and GCD tests were performed on a Bio-logic VMP3 multichannel electrochemical station and a Land CT2001 battery tester, respectively. CV tests of the prepared MnO_2 cathode were also carried out in a three-electrode system, in which a platinum plate as the counter electrode, a saturated calomel electrode (SCE) as the reference electrode, and 50 mL electrolyte was applied.

2.3 Material Characterizations

Microstructure and composition were characterized by XRD (Rigaku 2500) with Cu-Kα radiation operating at 40 kV and 100 mA within an angle range of 10° to 70° at a scan speed of 5° min^{-1}. Micro-morphology was observed by field emission scanning electron microscopy (SEM, Zeiss Supra 55) and TEM (Tecnai G2 F30). Element content in electrodes and electrolytes was analyzed by inductively coupled plasma atomic emission spectrometry (ICP-AES).

3 Results and Discussion

3.1 Characterization of MnO_2

The MnO_2 material used in this work was synthesized through a chemical co-precipitation method. XRD pattern and micro-morphology observations in Fig. 1a–c show that the synthesized MnO_2 powder is crystalline α-MnO_2 nanorod with a diameter of 10–60 nm and length of several hundred nanometers. From the XRD pattern in Fig. 1a, it seems that the strongest peak is the one at ~ 12.8°, but if the background is taken into account, the strongest peak is still the one at ~ 37.5°, which matches well with the α-MnO_2 (PDF# 44-0141). In addition, since the as-prepared sample is nanobelts, (110) plane (corresponding to the diffraction peak at ~ 12.8°) is considered as preferred orientation, thus leading to high diffraction intensity. A similar phenomenon was also observed for some other MnO_2 nanomaterials [38]. From the high-resolution TEM (HRTEM) image in Fig. 1d, the crystal planes (121) and (330) of the α-MnO_2 with a corresponding interplanar spacing of 0.238 nm and 0.233 nm respectively are observed, and high crystallinity of the as-synthesized α-MnO_2 sample is also confirmed.

3.2 Electrochemical Analysis

We first studied the electrochemical behaviors of MnO_2 cathode in two different electrolytes, including 50 mL 2 M $ZnSO_4$ (Fig. 2a) and 50 mL 2 M $ZnSO_4$ + 0.5 M $MnSO_4$ mixture solution (Fig. 2b–d). The capacity and rate performance of the MnO_2 cathode in $ZnSO_4$ + $MnSO_4$ electrolyte are exhibited in Fig. S1. Note that MnO_2 cathode would dissolve in $ZnSO_4$ electrolyte during charge/discharge processes, as detected by ICP-AES tests in Table S1. (This has also been pointed out in previous researches.) [37] With the addition of Mn^{2+} in the electrolyte, the redox peaks in CV curves (except for the 1st CV cycle) in Fig. 2a, b become

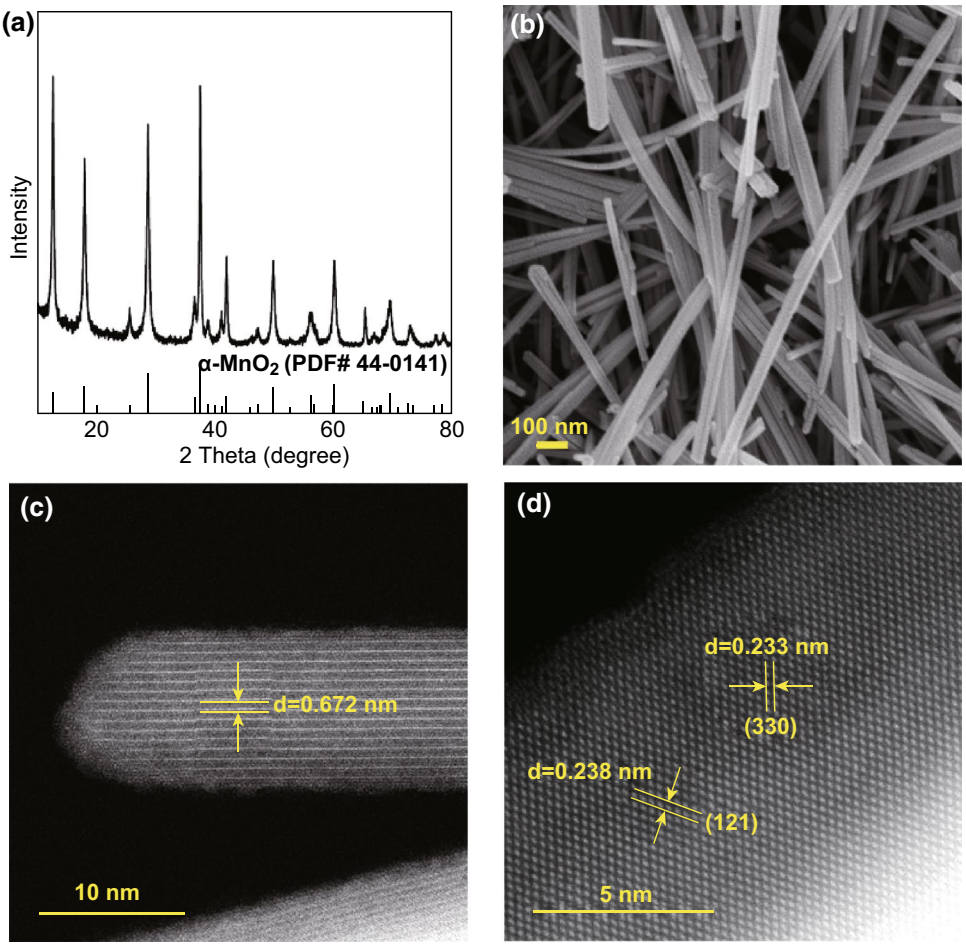

Fig. 1 **a** XRD pattern, **b** SEM image, **c** STEM, and **d** HRSTEM images of the synthesized MnO_2 nanorods

more obvious, and meanwhile, the gap between oxidation peak and reduction peak becomes smaller, which indicates that the reversibility of electrochemical process gets better. In Fig. 2a, the reduction peak is much stronger than the oxidation peak in the first cycle, which means that discharge products cannot be electrochemically oxidized completely. By contrast, the intensity of the reduction peak is close to that of the oxidation peak in Fig. 2b. Above phenomenon suggests that Mn^{2+} concentration in electrolyte plays a crucial role in the first discharge/charge process [48]. There are two pairs of redox peaks when the electrode discharges/charges in the 2 M $ZnSO_4$ + 0.5 M $MnSO_4$ electrolyte (Fig. 2b). The reduction peaks at low and high potentials are denoted as R_1 and R_2, respectively, and the oxidation peaks at low and high potentials are denoted as O_1 and O_2, respectively. Considering that electro-deposition of Mn^{2+} will occur only when the cathode potential reaches about 0.8 V versus SCE at the constant current of 0.1 A cm^{-2} (Fig. S2), the oxidation reactions of O_1 and O_2 ranging from 0.5 to 0.65 V versus SCE (Fig. 2b) are not caused by the electrodeposition of Mn^{2+}. This confirms that the preclusion of MnO_2 dissolution by Mn^{2+} in the electrolyte should be the dominant reason for good reversibility of discharge/charge processes in 2 M $ZnSO_4$ + 0.5 M $MnSO_4$ electrolyte.

There is a dip and a platform in the initial GCD curve (Fig. 2c) and the reaction type of R_1 (at about 1.2 V) and R_2 (at about 1.4 V) are further studied by the constant voltage discharge test (Fig. 2d). The current changes greatly when the battery is discharged at 1.2 V at which R_1 will happen, and it keeps almost flat when discharged at 1.4 V at which R_2 will occur. This indicates that a heterogeneous reaction occurs during R_1 and a homogeneous reaction occurs during R_2. Such a heterogeneous reaction between solid phases accompanying with nucleation process and

 https://doi.org/10.1007/s40820-019-0278-9

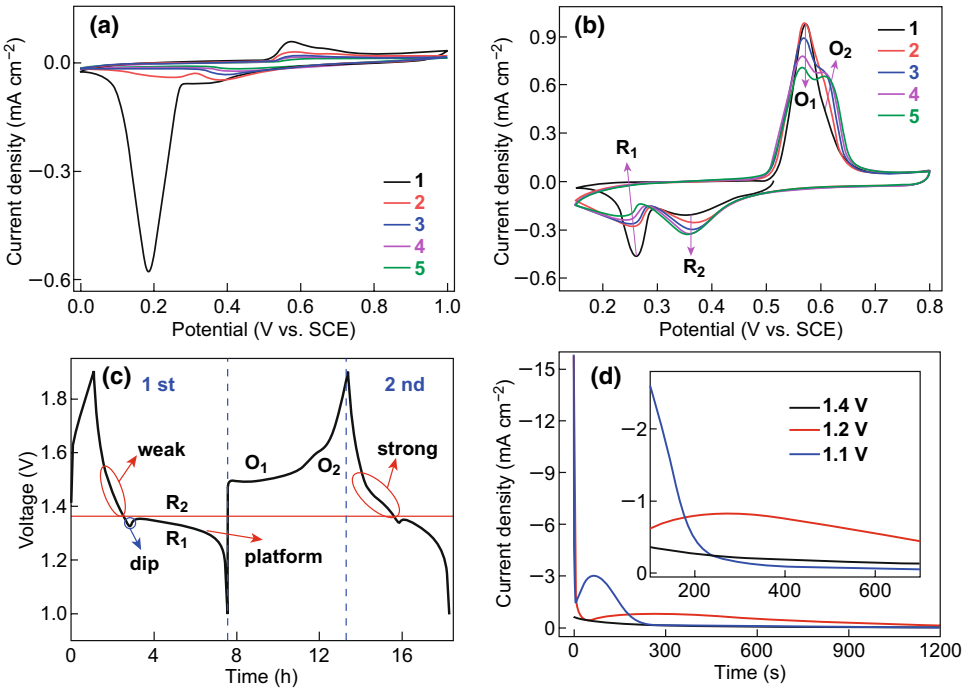

Fig. 2 Electrochemical behaviors of the prepared cathodes: **a** CV curves in 50 mL 2 M $ZnSO_4$ solution (first to fifth cycles); **b** CV (first to fifth cycles) and **c** GCD curves in 50 mL 2 M $ZnSO_4$ + 0.5 M $MnSO_4$ solution; **d** constant voltage discharge at various voltages (1.4, 1.2, and 1.1 V) and local magnification diagram (the inset)

electro-crystallization process will cause the formation of the dip and steep curve in the discharge curve in Fig. 2c [49]. With the increasing CV cycles (Fig. 2b), the peak current intensity of R_1 and O_1 is getting weaker, while the peak current intensity of R_2 and O_2 becomes stronger. Therefore, the redox reactions R_1/O_1 and R_2/O_2 are more likely to be independent of each other. That the initial process differs from the subsequent one can also be seen from Fig. 2c (the red circle). R_2 is weaker in the initial discharge process than that in the second one, which indicates that a new phase may generate as active materials.

3.3 Phase Evolution of Cathode in the Initial Discharge Process

ex situ XRD tests of the cathodes at different charge/discharge states support were performed. As shown in Fig. S3, when the cathode is initially discharged from 1.9 to 1.4 V, no new phase produces, while the cathode is further discharged to 1.0 V, several new diffraction peaks occur, indicating the appearance of new phases. In the charging process, some diffraction peaks cannot be detected, which means the disappearance of some phases. After 100 charges/discharge cycles, the XRD pattern is not in conformity with the XRD patterns of the cathode at the original state and fully charged state in the 1st charge process. These demonstrate that the cathode undergoes a complicated phase evolution. In the following, phase evolution of MnO_2 cathodes during the 1st discharge process, the 1st charge process and subsequent discharge/charge processes were investigated in detail.

To investigate phases evolution of cathode in the initial discharge process in 2 M $ZnSO_4$ + 0.5 M $MnSO_4$ electrolyte, R_1 and R_2 reactions (as defined in Fig. 2, the same hereinafter) are separately studied. Only R_2 occurs when the voltage of the battery is above 1.4 V. No new phase produces are seen from the XRD pattern (Fig. 3a). Nevertheless, characteristic peaks of the MnO_2 active material such as the peaks at 28° and 38° shift (inset of Fig. 3a), which is attributed to the change of the layer spacing of MnO_2. This means that the active material undergoes structure change. The nanorods become shorter (Fig. 3b) which is greatly different from that of the as-prepared material (Fig. 1b). Energy dispersive spectrometer (EDS)

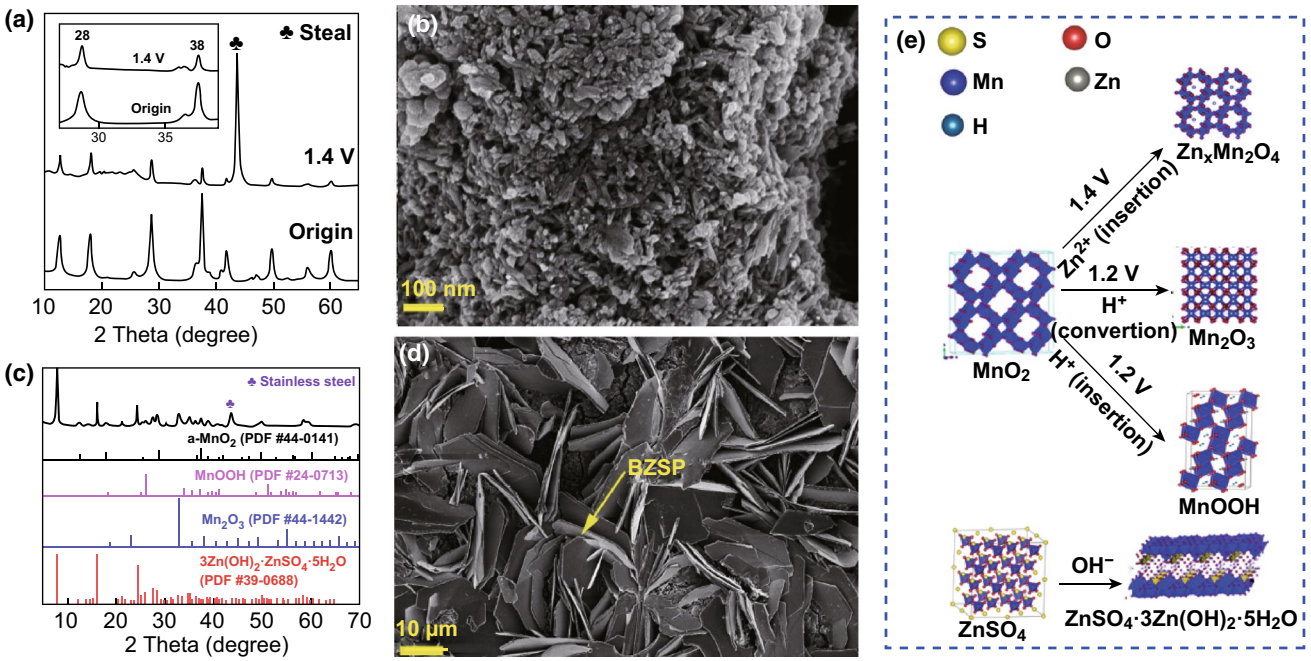

Fig. 3 The results of the cathode which is constant current discharged to 1.4 V and then constant voltage discharged at 1.4 V in 2 M $ZnSO_4$ + 0.5 M $MnSO_4$ electrolyte for 2 h: **a** XRD pattern and locally enlarged image (the inset); **b** SEM image of the surface of the cathode. Another cathode which is constant current discharged to 1.0 V: **c** XRD pattern; **d** SEM image of the surface of the cathode; **e** phase evolution of cathode during the first discharge process

analysis in Fig. S4 suggests that the molar ratio of Zn, Mn, and S is approximately 1:16:0. To exclude the influence of electrolyte's absorption, we immersed the electrodes in 2 M $ZnSO_4$ for 48 h and washed several times with deionized water. Neither Zn nor S element is found in the SEM–EDS result (Fig. S5). Thus, the existence of Zn in the cathode when discharging to 1.4 V is caused by the insertion of zinc ions in MnO_2, instead of zinc ion adsorption on the cathode surface. In other words, zinc ion insertion happens when the voltage of the Zn/MnO_2 battery is above 1.4 V. The process of zinc-ion insertion in MnO_2 can be written as:

$$MnO_2 + xZn^{2+} + 2xe^- \rightarrow Zn_xMnO_2 \quad (1)$$

R_1 reaction is then studied. When the battery is discharged to 1.2 V and then to the 1 V at constant current several new phases (XRD patterns in Fig. 3c) appear, which are confirmed as BZSP (PDF#39-0688), α-MnOOH (PDF#24-0713), and α-Mn_2O_3 (PDF#44-1442). There are many large hexagonal nanosheets in the SEM image (Fig. 3d). The Zn, O, and S element distribute evenly over the whole hexagonal nanosheets (Fig. S6b, c, e, f). And the atomic proportion of Zn to S is about 4:1 from the SEM–EDS results (Fig. S6d). Combined with the XRD result, we conclude that the hexagonal nanosheets are BZSP. The structure evolution of cathode in the first discharge is shown in Fig. 3e. The existence of α-MnOOH and α-Mn_2O_3 is further demonstrated by HRTEM (Fig. 4). The α-Mn_2O_3 is semi-coherent with the α-MnOOH phase (Fig. 4c). These substances and their reactions can be written as [21, 28, 37]:

$$4Zn^{2+} + SO_4^{2-} + 5H_2O + 6OH^- \rightarrow ZnSO_4 \cdot 3Zn(OH)_2 \cdot 5H_2O \quad (2)$$

$$MnO_2 + H^+ + e^- \rightarrow MnOOH \quad (3)$$

$$2MnO_2 + 2H^+ + 2e^- \rightarrow Mn_2O_3 + H_2O \quad (4)$$

Phases in regions **e**, **f**, **g**, and **h** in Fig. 4c, d marked by yellow dash can be identified as α-MnOOH, α-Mn_2O_3, α-Mn_2O_3, and α-Zn_xMnO_2, respectively, through fast Fourier transform (FFT) in Fig. 4e–h (detailed calculation procedures are given in Table S2–S4). From the TEM-EDS result, the Zn element can be found in both regions A and B and there is no S element in these regions (Fig. 4b), further confirming that zinc-ion inserts into the nanorods. Besides, the generation of BZSP and α-MnOOH indicates that H^+ and Zn^{2+} participate in the reaction. From the above discussions, zinc ion insertion in α-MnO_2 occurs around 1.4 V versus Zn^{2+}/Zn to generate α-Zn_xMnO_2, and proton conversion reaction

https://doi.org/10.1007/s40820-019-0278-9

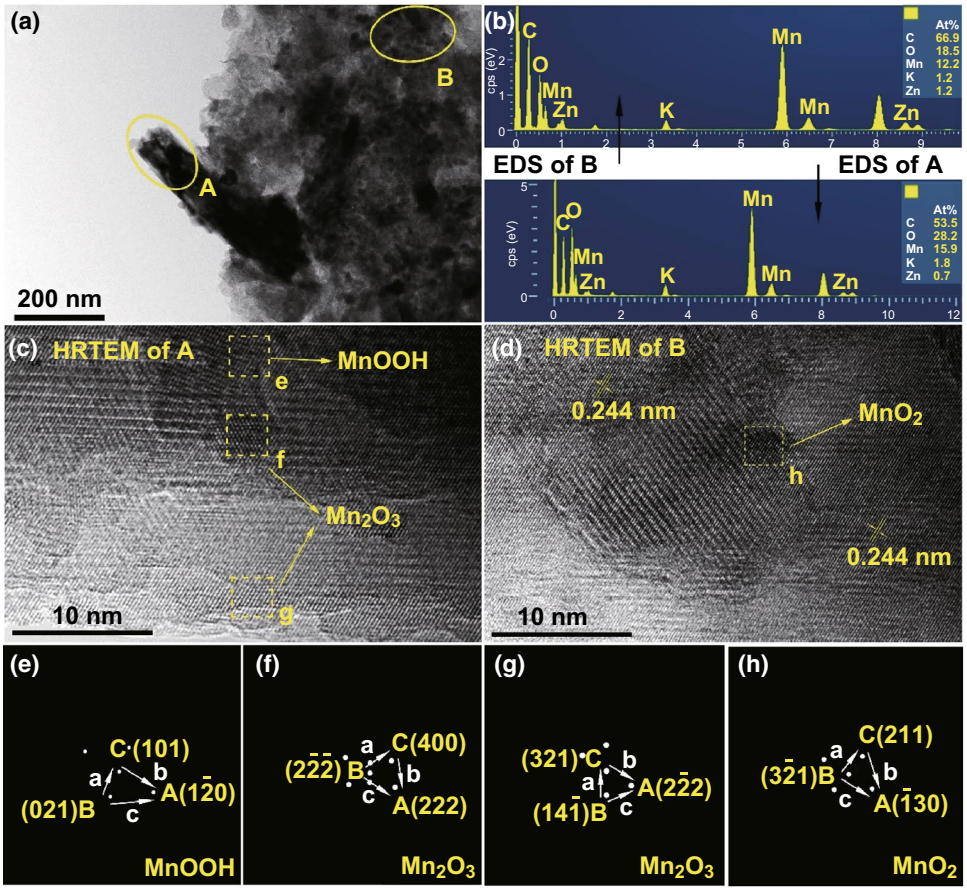

Fig. 4 TEM, HRTEM image, and TEM-EDS spectrum of the sample constant current discharge to 1.0 V: **a** TEM image **b** TEM-EDS spectrum result of region A and B marked in **a**. **c, d** HRTEM image of region A and B marked in Fig. 4a, respectively. **e, f** FFT of the region marked by a yellow dash in **c** and **d**, respectively

happens between 1.0 and 1.3 V in the cathode and leads to the generation of MnOOH, Mn_2O_3, and BZSP.

3.4 Phase Evolution of Cathode in the First Charge Process

To detect the phase evolution of MnO_2 cathode during the charge process, the battery is discharged to 1.0 V and then charged to 1.9 V in 2 M $ZnSO_4$ and 2 M $ZnSO_4$ + 0.5 M $MnSO_4$ electrolyte, respectively. The discharging products of Mn_2O_3, BZSP, and MnO_2 still exist on the charged cathode, and besides, new phase $ZnMn_3O_7{\cdot}3H_2O$ generates (Fig. 5a). It is worth noting that when adding Mn^{2+} in the electrolyte, the diffraction peaks of $ZnMn_3O_7{\cdot}3H_2O$ become strong while the diffraction peaks of BZSP become weak (Fig. 5a). The morphology of cathode changes greatly (from hexagonal nanosheets to ball-like nanoflowers) during the initial charging process as shown in Figs. S7a–f and S8a–d. Figure S7a–f shows that BZSP exists in the 2 M $ZnSO_4$ solution while almost disappears in 2 M $ZnSO_4$ + 0.5 M $MnSO_4$ solution during the charging process. It means that added Mn^{2+} in the electrolyte can promote the dissolution of BZSP. To confirm this, the fresh cathode was discharged to 1.0 V in 2 M $ZnSO_4$ + 0.5 M $MnSO_4$ solution and then soaked in potassium hydrogen phthalate solution (pH = 4.0) for 72 h to completely dissolve BZSP. The electrode without BZSP was then charged in 2 M $ZnSO_4$ + 0.5 M $MnSO_4$ electrolyte. Meanwhile, the discharged electrode with BZSP was separately charged in the electrolytes of 2 M $ZnSO_4$ and 2 M $ZnSO_4$ + 0.5 M $MnSO_4$. The charge processes of the three conditions are shown in Fig. 5b. It can be seen that the platform, which means heterogeneous reaction happens, occurs at 1.5 V only when BZSP and Mn^{2+} both exist. To further confirm this, a discharged electrode with

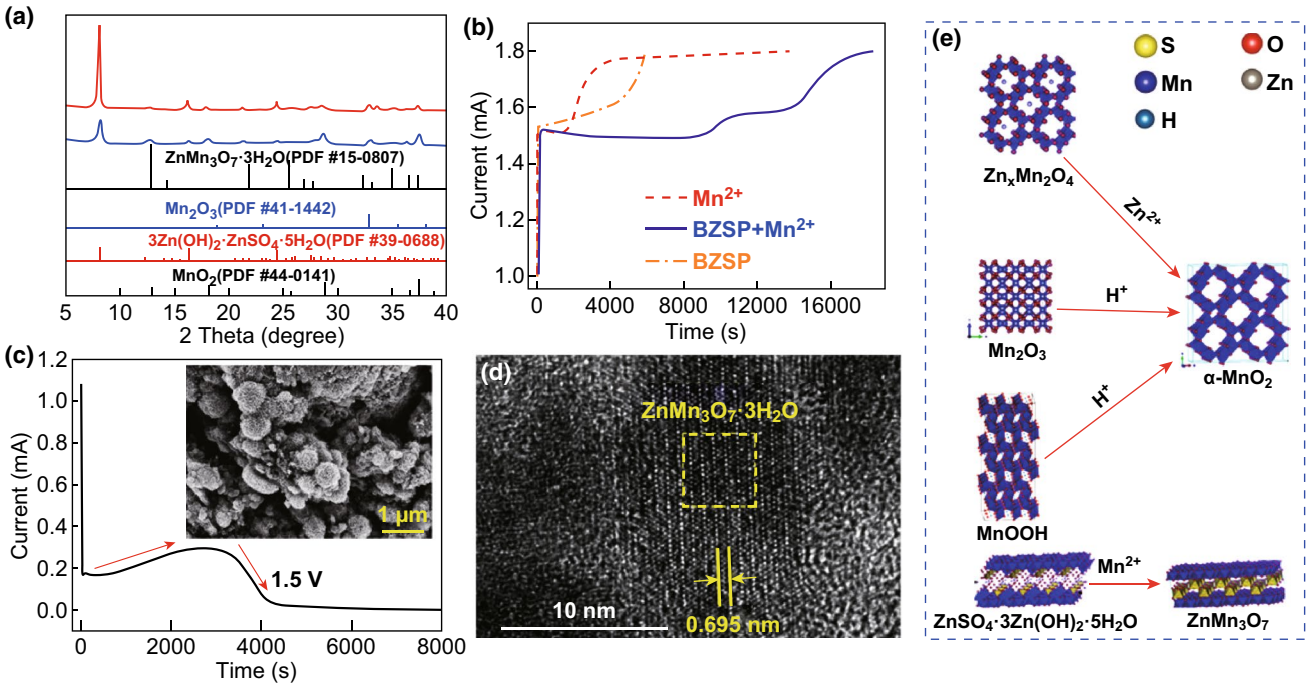

Fig. 5 The first charge process: **a** XRD pattern of the fully charged cathode in the first charge process; **b** charging curves of α-MnO_2 electrodes after discharge to 1 V in different cases; **c** constant voltage test; **d** HRTEM image and analysis result. **e** Phase evolution of cathode during the first charge process

BZSP charge at 1.5 V in the 2 M $ZnSO_4$ + 0.5 M $MnSO_4$ solution. The nanoflower-like product generates (inset in Fig. 5c) as expected. $ZnMn_3O_7{\cdot}3H_2O$ is also found in HRTEM in Fig. 5d. Combining with the result of XRD, the nanoflower is $ZnMn_3O_7{\cdot}3H_2O$. The dissolution of BZSP (nanosheets in Fig. S8a–d) and the occurrence of the new phase (nanoflowers in Fig. S8a–b) $ZnMn_3O_7{\cdot}3H_2O$ indicate that $ZnMn_3O_7{\cdot}3H_2O$ generate from the conversion reaction between BZSP and Mn^{2+}. The nanoflower is $Zn(OH)_2$ and MnO_2 alternately layered structure as seen from Fig. S9. The conversion reactions are as follows: Zn^{2+} in the interlayer of $Zn(OH)_2$ (Fig. S10) exchanges with Mn^{2+} and then the Mn^{2+} is chemically oxidized during the charging process. With continuous oxidation of Mn^{2+}, the Mn^{2+} reacts with H_2O to generate $ZnMn_3O_7{\cdot}3H_2O$ (Fig. S10). The structure evolution of cathode in the first charge is shown in Fig. 5e. In other words, besides H^+ and Zn^{2+}, Mn^{2+} also participates in the reactions that occur during the discharge/charge process as the conversion reactions are supposed as follows:

$$3(ZnSO_4 \cdot 3Zn(OH)_2 \cdot 5H_2O) + 3Mn^{2+} + 8e^- \rightarrow ZnMn_3O_7 \cdot 3H_2O + 3ZnSO_4 + 18OH^- + 8Zn^{2+} + 12H_2O \quad (5)$$

The generation of $ZnMn_3O_7{\cdot}3H_2O$ during the first charge process can explain the phenomenon that the second discharge curve of the battery is different from the first discharge curve. In a word, during the first charging process, Zn_xMnO_2 and MnOOH reversibly become α-MnO_2 with the extraction of Zn^{2+} and H^+, while $ZnMn_3O_7{\cdot}3H_2O$ acts as the host for the insertion of Zn^{2+} forms through the reaction between Mn^{2+} and BZSP.

3.5 Phase Evolution of Cathode in Subsequent Discharge/Charge Processes

The phases of the battery system after 100 charges/discharge cycles are also studied. XRD patterns of the discharged cathode after 100 cycles in 2 M $ZnSO_4$ + 0.5 M $MnSO_4$ solution in Fig. 6a imply that the main phases of the system are $ZnMn_2O_4$ (PDF#24-1133), $Zn_2Mn_3O_8$ (PDF#32-1472), Mn_2O_3, BZSP, and α-MnO_2. These components are confirmed in HRTEM images in Fig. 6b–d. As a contrast, the battery in the 2 M $ZnSO_4$ solution, the main phases of the system are $ZnMn_2O_4$, $ZnMn_3O_7$, Mn_2O_3, and BZSP (Fig. S11a, b). $ZnMn_2O_4$ is on the surface of the α-MnO_2 in HRTEM (Fig. 6b), so it may be

 https://doi.org/10.1007/s40820-019-0278-9

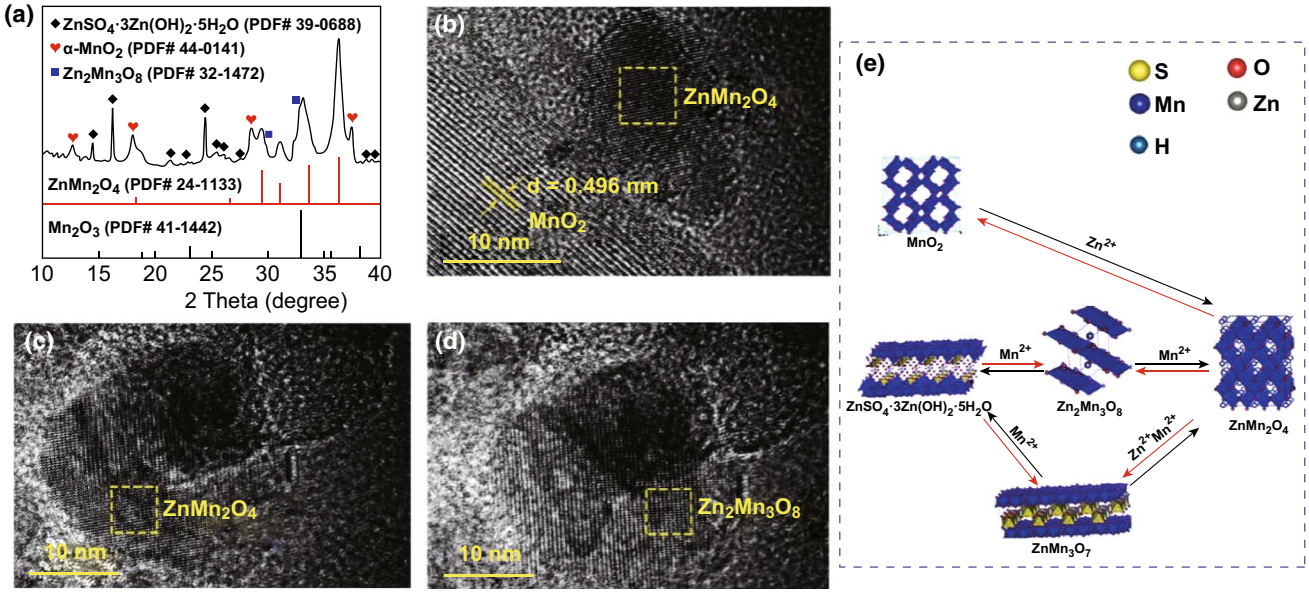

Fig. 6 The MnO_2 cathode after 100 charge/discharge cycles in 2 M $ZnSO_4$ + 0.5 M $MnSO_4$ electrolyte: **a** XRD patterns; **b–d** HRTEM images; **e** phase evolution of cathode during the repeated charge/discharge processes after the first charge/discharge cycle

converted from α-MnO_2. $Zn_2Mn_3O_8$ and $ZnMn_2O_4$ are coherent in the HRTEM (Fig. 6c, d). Thus, $Zn_2Mn_3O_8$ reacts with Mn^{2+} to form $ZnMn_2O_4$. (This will be further analyzed in the Mn–Zn–O diagram in the following part.) There are two kinds of nanoparticles after 100 cycles (Fig. S12), which may be converted from BZSP and Mn^{2+} as nanosheets and nanoparticles surround each other. Combining the XRD result (Fig. 6a), the phase is $Zn_2Mn_3O_8$. Thus, $Zn_2Mn_3O_8$ is generated from the reactions between BZSP and Mn^{2+}. The structure evolution of cathode after 100 cycles is shown in Fig. 6e. Reactions between them are as follows:

$$Zn_xMnO_2 + (0.5 - x)Zn^{2+} + (1 - 2x)e^- \rightarrow 0.5ZnMn_2O_4 \quad (6)$$

$$Zn_2Mn_3O_8 + Mn^{2+} \rightarrow 2ZnMn_2O_4 \quad (7)$$

To sum up, within the continuous charge/discharge process, $ZnMn_2O_4$ and $Zn_2Mn_3O_8$ as host for insertion of Zn^{2+} further generate on the surface of MnO_2, which implies that the phase change of MnO_2 cathode is irreversible.

3.6 Thermodynamic Analysis

When dynamic conditions are met, the phases can be predicted from Zn-Mn–O diagram since the system of the Zn/$ZnSO_4$ + $MnSO_4$/MnO_2 battery reaches an equilibrium state after a certain cycle. The isothermal cross section of the phase diagram (25 °C) is shown in Fig. 7a. Since MnO_2 is used as an active material and $ZnSO_4$ + $MnSO_4$ as the electrolyte for the beginning, the phase of the reaction is bound to three elements (Mn, O, and Zn). When the thermodynamic stability of the system reaches, the definite phases include manganese oxide (MnO_2, Mn_2O_3, Mn_3O_4, and MnO) and zinc manganese oxide ($ZnMn_2O_4$ and $Zn_2Mn_3O_8$) (Fig. 7a). Detailed density functional theory calculation and theoretical analysis of MnO_2 as a cathode of ZIBs are given in Discussion S1 and S2 in Supporting Information). There are two paths to the reduction of MnO_2: (i) $MnO_2 \rightarrow Mn_2O_3 \rightarrow Mn_3O_4 \rightarrow MnO$, in which path there is no Zn involvement; (ii) $MnO_2 \rightarrow ZnMn_2O_4$ with Zn involvement. For Mn_2O_3 oxidation, it is directly oxidized to MnO_2: $Mn_2O_3 \rightarrow MnO_2$. The oxidation of $ZnMn_2O_4$ has two paths: Zn extracts out completely from $ZnMn_2O_4$ to generate MnO_2 or Mn partially removes from $ZnMn_2O_4$ to generate $Zn_2Mn_3O_8$. They can express as: (1) $ZnMn_2O_4 \rightarrow MnO_2$; (2) $ZnMn_2O_4 \rightarrow Zn_2Mn_3O_8$. And there's only one way for the $Zn_2Mn_3O_8$ reduction: $Zn_2Mn_3O_8 \rightarrow ZnMn_2O_4$. In the Zn/$ZnSO_4$ + $MnSO_4$/α-MnO_2 system studied in this paper, MnO dissolves in the electrolyte or can be inhibited when there is a certain concentration of Mn^{2+}. Thus, there are five kinds of phases that may exist, such as MnO_2, Mn_2O_3, Mn_3O_4, $ZnMn_2O_4$, and $Zn_2Mn_3O_8$. When taking PH and potentials into consideration, MnO_2, Mn_2O_3, $ZnMn_2O_4$, MnOOH,

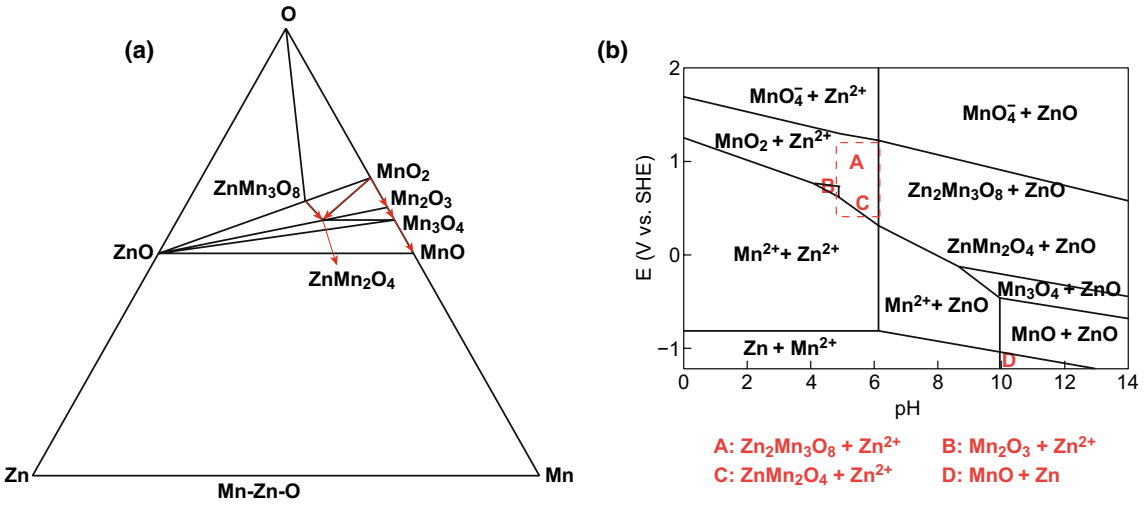

Fig. 7 **a** Zn–Mn–O diagram and **b** E-pH diagram of Zn–Mn–H_2O system

and $Zn_2Mn_3O_8$ can form in our system but MnOOH is not stable, which matches well with our work (the red region in Fig. 7b). The reaction route is concluded to be as follows: (1) $MnO_2 \rightarrow Mn_2O_3$, (2) $MnO_2 \rightarrow ZnMn_2O_4$ and (3) $Zn_2Mn_3O_8 \rightarrow ZnMn_2O_4$ (Fig. 7a). MnO_2, Mn_2O_3, $ZnMn_2O_4$, and $Zn_2Mn_3O_8$ are stable phases and all can store Zn^{2+} (Fig. 7b).

Overall, we combined electrochemical analysis, phase identification with E-pH diagram of the Mn–Zn–H_2O system together to analyze charge/discharge processes of aqueous rechargeable Zn//MnO_2 batteries and revealed complicated phase evolution of the cathode (i.e., what new phases will form and how can they form in different charge/discharge stages). We obtained some different conclusions from previous literature. For example, Sun et al. thought that the conversion of H^+ occurs before Zn^{2+} insertion [38]. But we find that Zn^{2+} insertion occurs before the conversion of H^+ in the first discharge process, and this is confirmed by thermodynamic analysis. Besides, previous literature deemed that the disappearance of BZSP is always caused by the change in electrolyte pH [34], but we find that BZSP can react with Mn^{2+} in the electrolyte to form a new phase of $ZnMn_3O_7$.

4 Conclusions

Based on experimental results and theoretical analysis of Zn/MnO_2 ZIBs with the mixture electrolyte of $ZnSO_4 + MnSO_4$ aqueous solution, we found that the mechanism in ZIBs is dynamic and the phase transformation at MnO_2 cathode is irreversible during charge/discharge processes. Not only H^+ and Zn^{2+} but also Mn^{2+} in the electrolyte take part in the reactions. In the first discharge process, Zn_xMnO_2, MnOOH, Mn_2O_3, and by-product BZSP generate, and then in the first charge process, α-MnO_2 and $ZnMn_3O_7{\cdot}3H_2O$ appear. In the following charge/discharge processes, $ZnMn_2O_4$ and $ZnMn_3O_8$ are further generated on the surface of MnO_2 and serve as the hosts for Zn^{2+} insertion. The mechanism becomes dynamic and complex because of the co-participation of the insertion process, conversion reaction, and oxidation reactions. The aforementioned phase changes inside ZIBs are well explained by the Mn–Zn–O phase diagram and the E-pH diagram. This work can provide guidance for continual research from the following aspects. (i) The research method combining electrochemical analysis and phase identification with E-pH diagram together can be used to analyze charge/discharge processes of other electrochemical energy storage systems, such as aqueous rechargeable Zn//V_2O_5 batteries. (ii) According to the proposed energy storage systems in this work, at least two approaches can be applied to enhance cycling performance of ZIBs: One is adding Mn^{2+} to promote the disappearance of BZSP, and the other one is adding pH buffer into the electrolytes or preparing solid electrolytes to prohibit the generation of OH– and BZSP.

Acknowledgements The authors appreciate the financial support from the International Science & Technology Cooperation Program of China (No. 2016YFE0102200), Shenzhen Technical Plan Project (No. JCYJ20160301154114273), National Key Basic Research

 https://doi.org/10.1007/s40820-019-0278-9

(973) Program of China (No. 2014CB932400), and Local Innovative and Research Teams Project of Guangdong Pearl River Talents Program (2017BT01N111).

Electronic supplementary material The online version of this article (https://doi.org/10.1007/s40820-019-0278-9) contains supplementary material, which is available to authorized users.

References

1. T.-H. Kim, J.-S. Park, S.K. Chang, S. Choi, J.H. Ryu, H.-K. Song, The current move of lithium-ion batteries towards the next phase. Adv. Energy Mater. **2**, 860–872 (2012). https://doi.org/10.1002/aenm.201200028
2. B. Dunn, H. Kamath, J.M. Tarascon, Electrical energy storage for the grid: a battery of choices. Science **334**, 928–935 (2011). https://doi.org/10.1126/science.1212741
3. H. Sun, J.-G. Wang, Y. Zhang, W. Hua, Y. Li, H. Liu, Ultrafast lithium energy storage enabled by interfacial construction of interlayer-expanded MoS_2/N-doped carbon nanowires. J. Mater. Chem. A **6**, 13419–13427 (2018). https://doi.org/10.1039/C8TA04852E
4. J.-G. Wang, H. Liu, R. Zhou, X. Liu, B. Wei, Onion-like nanospheres organized by carbon encapsulated few-layer MoS_2 nanosheets with enhanced lithium storage performance. J. Power Sources **413**, 327–333 (2019). https://doi.org/10.1016/j.jpowsour.2018.12.055
5. C. Delmas, M. Maccario, L. Croguennec, F. Le Cras, F. Weill, Lithium deintercalation in $LiFePO_4$ nanoparticles via a domino-cascade model. Nat. Mater. **7**, 665–671 (2008). https://doi.org/10.1038/nmat2230
6. N. Alias, A.A. Mohamad, Advances of aqueous rechargeable lithium-ion battery: a review. J. Power Sources **274**, 237–251 (2015). https://doi.org/10.1016/j.jpowsour.2014.10.009
7. J.O.G. Posada, A.J.R. Rennie, S.P. Villar, V.L. Martins, J. Marinaccio et al., Aqueous batteries as grid-scale energy storage solutions. Renew. Sustain. Energy Rev. **68**, 1174–1182 (2017). https://doi.org/10.1016/j.rser.2016.02.024
8. C. Xu, B. Li, H. Du, F. Kang, Energetic zinc ion chemistry: the rechargeable zinc ion battery. Angew. Chem. Int. Ed. **51**, 933–935 (2012). https://doi.org/10.1002/anie.201106307
9. L. Zhang, L. Chen, X. Zhou, Z. Liu, Towards high-voltage aqueous metal-ion batteries beyond 1.5 V: the zinc/zinc hexacyanoferrate system. Adv. Energy Mater. **5**, 1400930 (2015). https://doi.org/10.1002/aenm.201400930
10. R. Trocoli, F. La Mantia, An aqueous zinc-ion battery based on copper hexacyanoferrate. Chemsuschem **8**, 481–485 (2015). https://doi.org/10.1002/cssc.201403143
11. Z. Liu, G. Pulletikurthi, F. Endres, A prussian blue/zinc secondary battery with a bio-ionic liquid-water mixture as electrolyte. ACS Appl. Mater. Interfaces **8**, 12158–12164 (2016). https://doi.org/10.1021/acsami.6b01592
12. Y. Wu, Y. Yang, X. Zhao, Y. Tan, Y. Liu, Z. Wang, F. Ran, A novel hierarchical porous 3D structured vanadium nitride/carbon membranes for high-performance supercapacitor negative electrodes. Nano-Micro Lett. **10**, 63 (2018). https://doi.org/10.1007/s40820-018-0217-1
13. Y. Yang, Y. Tang, G. Fang, L. Shan, J. Guo et al., Li^+ intercalated $V_2O_5{\cdot}nH_2O$ with enlarged layer spacing and fast ion diffusion as an aqueous zinc-ion battery cathode. Energy Environ. Sci. **11**, 3157–3162 (2018). https://doi.org/10.1039/C8EE01651H
14. J.H. Jo, Y.-K. Sun, S.-T. Myung, Hollandite-type al-doped $VO_{1.52}(OH)_{0.77}$ as a zinc ion insertion host material. J. Mater. Chem. A **5**, 8367–8375 (2017). https://doi.org/10.1039/C7TA01765K
15. X. Guo, G. Fang, W. Zhang, J. Zhou, L. Shan et al., Mechanistic insights of Zn^{2+} storage in sodium vanadates. Adv. Energy Mater. **18**, 1801819 (2018). https://doi.org/10.1002/aenm.201801819
16. D. Kundu, B.D. Adams, V. Duffort, S.H. Vajargah, L.F. Nazar, A high-capacity and long-life aqueous rechargeable zinc battery using a metal oxide intercalation cathode. Nat. Energy **1**, 16119 (2016). https://doi.org/10.1038/nenergy.2016.119
17. C.W. Mason, F. Lange, Aqueous ion battery systems using sodium vanadium phosphate stabilized by titanium substitution. ECS Electrochem. Lett. **4**, A79–A82 (2015). https://doi.org/10.1149/2.0011508eel
18. H.B. Zhao, C.J. Hu, H.W. Cheng, J.H. Fang, Y.P. Xie et al., Novel rechargeable $M_3V_2(PO_4)_3$//zinc (M = Li, Na) hybrid aqueous batteries with excellent cycling performance. Sci. Rep. **6**, 25809 (2016). https://doi.org/10.1038/srep25809
19. B. Tang, G. Fang, J. Zhou, L. Wang, Y. Lei, C. Wang, T. Lin, Y. Tang, S. Liang, Potassium vanadates with stable structure and fast ion diffusion channel as cathode for rechargeable aqueous zinc-ion batteries. Nano Energy **51**, 579–587 (2018). https://doi.org/10.1016/j.nanoen.2018.07.014
20. B. Zhang, Y. Liu, X. Wu, Y. Yang, Z. Chang, Z. Wen, Y. Wu, An aqueous rechargeable battery based on zinc anode and $Na_{0.95}MnO_2$. Chem. Commun. **50**, 1209–1211 (2014). https://doi.org/10.1039/C3CC48382G
21. N. Zhang, F. Cheng, Y. Liu, Q. Zhao, K. Lei, C. Chen, X. Liu, J. Chen, Cation-deficient spinel $ZnMn_2O_4$ cathode in $Zn(CF_3SO_3)_2$ electrolyte for rechargeable aqueous Zn-ion battery. J. Am. Chem. Soc. **138**, 12894–12901 (2016). https://doi.org/10.1021/jacs.6b05958
22. G. Yuan, J. Bai, T.N.L. Doan, P. Chen, Synthesis and electrochemical investigation of nanosized $LiMn_2O_4$ as cathode material for rechargeable hybrid aqueous batteries. Mater.

Lett. **137**, 311–314 (2014). https://doi.org/10.1016/j.matlet.2014.09.019

23. J. Zhao, Y. Li, X. Peng, S. Dong, J. Ma, G. Cui, L. Chen, High-voltage Zn/$LiMn_{0.8}Fe_{0.2}PO_4$ aqueous rechargeable battery by virtue of "water-in-salt" electrolyte. Electrochem. Commun. **69**, 6–10 (2016). https://doi.org/10.1016/j.elecom.2016.05.014
24. G. Fang, C. Zhu, M. Chen, J. Zhou, B. Tang, X. Cao, X. Zheng, A. Pan, S. Liang, Suppressing manganese dissolution in potassium manganate with rich oxygen defects engaged high-energy-density and durable aqueous zinc-ion battery. Adv. Funct. Mater. **29**, 1808375 (2019). https://doi.org/10.1002/adfm.201808375
25. J. Lee, J.B. Ju, W.I. Cho, B.W. Cho, S.H. Oh, Todorokite-type MnO_2 as a Zinc-ion intercalating material. Electrochim. Acta **112**, 138–143 (2013). https://doi.org/10.1016/j.electacta.2013.08.136
26. T. Yamamoto, T. Shoji, Rechargeable Zn–$ZnSO_4$–MnO_2-type cells. Inorg. Chim. Acta **117**, L27–L28 (1986). https://doi.org/10.1016/S0020-1693(00)82175-1
27. M.H. Alfaruqi, S. Islam, J. Gim, J. Song, S. Kim et al., A high surface area tunnel-type α- MnO_2 nanorod cathode by a simple solvent-free synthesis for rechargeable aqueous zinc-ion batteries. Chem. Phys. Lett. **650**, 64–68 (2016). https://doi.org/10.1016/j.cplett.2016.02.067
28. M.H. Alfaruqi, J. Gim, S. Kim, J. Song, D.T. Pham, J. Jo, Z. Xiu, V. Mathew, J. Kim, A layered δ-MnO_2 nanoflake cathode with high zinc-storage capacities for eco-friendly battery applications. Electrochem. Commun. **60**, 121–125 (2015). https://doi.org/10.1016/j.elecom.2015.08.019
29. G. Fang, J. Zhou, A. Pan, S. Liang, Recent advances in aqueous zinc-ion batteries. ACS Energy Lett. **3**, 2480–2501 (2018). https://doi.org/10.1021/acsenergylett.8b01426
30. P. He, M. Yan, G. Zhang, R. Sun, L. Chen, Q. An, L. Mai, Layered VS_2 nanosheet-based aqueous Zn ion battery cathode. Adv. Energy Mater. **7**, 601920 (2017). https://doi.org/10.1002/aenm.201601920
31. Y. Cheng, L. Luo, L. Zhong, J. Chen, B. Li et al., Highly reversible zinc-ion intercalation into chevrel phase Mo_6S_8 nanocubes and applications for advanced zinc-ion batteries. ACS Appl. Mater. Interfaces **8**, 13673–13677 (2016). https://doi.org/10.1021/acsami.6b03197
32. M.H. Alfaruqi, V. Mathew, J. Gim, S. Kim, J. Song, J.P. Baboo, S.H. Choi, J. Kim, Electrochemically induced structural transformation in a γ-MnO_2 cathode of a high capacity zinc-ion battery system. Chem. Mater. **26**, 3609–3620 (2015). https://doi.org/10.1021/cm504717p
33. B. Lee, H.R. Lee, H. Kim, K.Y. Chung, B.W. Cho, S.H. Oh, Elucidating the intercalation mechanism of zinc ions into alpha-MnO_2 for rechargeable zinc batteries. Chem. Commun. **51**, 9265–9268 (2015). https://doi.org/10.1039/C5CC02585K
34. B. Lee, H.R. Seo, H.R. Lee, C.S. Yoon, J.H. Kim, K.Y. Chung, B.W. Cho, S.H. Oh, Critical role of pH evolution of electrolyte in the reaction mechanism for rechargeable zinc batteries. Chemsuschem **9**, 2948–2956 (2016). https://doi.org/10.1002/cssc.201600702
35. B. Lee, C.S. Yoon, H.R. Lee, K.Y. Chung, B.W. Cho, S.H. Oh, Electrochemically-induced reversible transition from the tunneled to layered polymorphs of manganese dioxide. Sci. Rep. **4**, 6066 (2014). https://doi.org/10.1038/srep06066
36. M.H. Alfaruqi, J. Gim, S. Kim, J. Song, J. Jo, S. Kim, V. Mathew, J. Kim, Enhanced reversible divalent zinc storage in a structurally stable α-MnO_2 nanorod electrode. J. Power Sources **288**, 320–327 (2015). https://doi.org/10.1016/j.jpowsour.2015.04.140
37. H. Pan, Y. Shao, P. Yan, Y. Cheng, K.S. Han et al., Reversible aqueous zinc/manganese oxide energy storage from conversion reactions. Nat. Energy **1**, 16039 (2016). https://doi.org/10.1038/nenergy.2016.39
38. W. Sun, F. Wang, S. Hou, C. Yang, X. Fan et al., Zn/MnO_2 battery chemistry with H^+ and Zn^{2+} coinsertion. J. Am. Chem. Soc. **139**, 9775–9778 (2017). https://doi.org/10.1021/jacs.7b04471
39. G.G. Yadav, J.W. Gallaway, D.E. Turney, M. Nyce, J. Huang, X. Wei, S. Banerjee, Regenerable Cu-intercalated MnO_2 layered cathode for highly cyclable energy dense batteries. Nat. Commun. **8**, 14424 (2017). https://doi.org/10.1038/ncomms14424
40. N. Jabeen, A. Hussain, Q. Xia, S. Sun, J. Zhu, H. Xia, High-performance 2.6 V aqueous asymmetric supercapacitors based on in situ formed $Na_{0.5}MnO_2$ nanosheet assembled nanowall arrays. Adv. Mater. **29**, 1700804 (2017). https://doi.org/10.1002/adma.201700804
41. A. Konarov, N. Voronina, J.H. Jo, Z. Bakenov, Y.-K. Sun, S.-T. Myung, Present and future perspective on electrode materials for rechargeable zinc-ion batteries. ACS Energy Lett. **3**, 2620–2640 (2018). https://doi.org/10.1021/acsenergylett.8b01552
42. M. Song, H. Tan, D. Chao, H.J. Fan, Recent advances in Zn-ion batteries. Adv. Funct. Mater. **28**, 1802564 (2018). https://doi.org/10.1002/adfm.201802564
43. J. Hao, J. Mou, J. Zhang, L. Dong, W. Liu, C. Xu, F. Kang, Electrochemically induced spinel-layered phase transition of Mn_3O_4 in high performance neutral aqueous rechargeable zinc battery. Electrochim. Acta **259**, 170–178 (2018). https://doi.org/10.1016/j.electacta.2017.10.166
44. D. Grujicic, B. Pesic, Reaction and nucleation mechanisms of copper electrodeposition from ammoniacal solutions on vitreous carbon. Electrochim. Acta **50**, 4426–4443 (2005). https://doi.org/10.1016/j.electacta.2005.02.012
45. A. Anderko, S.J. Sanders, R.D. Young, Real-solution stability diagrams: a thermodynamic tool for modeling corrosion in wide temperature and concentration ranges. Corrosion **53**, 43–53 (1997). https://doi.org/10.5006/1.3280432
46. A.G. Tyurin, A role of manganese in the corrosion and electrochemical behavior of stainless steels. Prot. Met. **41**, 68–75 (2005). https://doi.org/10.1007/s11124-005-0010-7
47. X. Zhou, C. Wei, M. Li, S. Qiu, X. Li, Thermodynamics of vanadium–sulfur–water systems at 298 K. Hydrometallurgy **106**, 104–112 (2011). https://doi.org/10.1016/j.hydromet.2010.12.003

 https://doi.org/10.1007/s40820-019-0278-9

48. M. Chamoun, W.R. Brant, C.-W. Tai, G. Karlsson, D. Noréus, Rechargeability of aqueous sulfate Zn/MnO_2 batteries enhanced by accessible Mn^{2+} ions. Energy Storage Mater. **15**, 351–360 (2018). https://doi.org/10.1016/j.ensm.2018.06.019

49. K.J. Vetter, A general thermodynamic theory of the potential of passive electrodes and its influence on passive corrosion. J. Electrochem. Soc. **110**, 597–605 (1963). https://doi.org/10.1149/1.2425837